

# Flexible organic photovoltaics based on water-processed silver nanowire electrodes

Yanna Sun<sup>1</sup>, Meijia Chang<sup>1</sup>, Lingxian Meng<sup>1</sup>, Xiangjian Wan<sup>1</sup>, Huanhuan Gao<sup>1</sup>, Yamin Zhang<sup>1</sup>, Kai Zhao<sup>1</sup>, Zhenhe Sun<sup>1</sup>, Chenxi Li<sup>1</sup>, Shuiren Liu<sup>2</sup>, Huike Wang<sup>2</sup>, Jiajie Liang<sup>2</sup> and Yongsheng Chen<sup>1\*</sup>

**A key feature of organic electronic devices is their mechanical flexibility. However, the performance of flexible organic optoelectronic devices still lags behind the performance of devices on rigid substrates. This is due, in particular, to the lack of flexible transparent electrodes that simultaneously offer low resistance, high transparency and a smooth surface. Here, we report flexible transparent electrodes created using water-processed silver nanowires and a polyelectrolyte. Due to ionic electrostatic charge repulsion, the nanowires form grid-like structures in a single step, leading to smooth, flexible electrodes that have a sheet resistance of around  $10 \Omega \square^{-1}$  and a transmittance of around 92% (excluding the substrate). To illustrate the potential of the approach in organic electronics, we use the flexible electrodes to create organic photovoltaic devices. The devices are tested with different types of donors and acceptors, and exhibit performance comparable to devices based on commercial rigid electrodes. Furthermore, flexible single-junction and tandem devices achieve power conversion efficiencies of 13.1% and 16.5%, respectively.**

Organic electronics offers a range of versatile features, including low-cost roll-to-roll production<sup>1,2</sup>, easy integration with other systems and device flexibility<sup>3,4</sup>. Recently, organic devices, including organic photovoltaics (OPVs)<sup>5–8</sup>, light-emitting diodes<sup>9</sup> and field-effect transistors<sup>10</sup>, have undergone considerable development and demonstrated promising application potential<sup>11–13</sup>. However, the performance of flexible organic optoelectronic devices still lags behind that of devices on rigid substrates/electrodes<sup>14,15</sup>. For example, power conversion efficiencies (PCEs) of over 17% have been achieved for OPV devices on indium tin oxide (ITO) electrodes<sup>6</sup>, but PCEs for flexible single-junction and tandem OPV devices have reached around 12% and 8%, respectively<sup>3,15–19</sup>. The key issue here is the absence of high-performance flexible transparent electrodes (FTEs) that can combine the necessary characteristics, which include flexibility, low resistance, high transparency and a smooth surface, and compatibility with the solution processes generally used in organic electronics<sup>15,20–22</sup>.

FTEs can be fabricated using dry methods (such as vacuum deposition using conducting metal or nano carbon materials)<sup>18,23</sup> or wet methods (solution processes such as slot die, ink-jet/nano printing, and electrospinning)<sup>24–26</sup>. Dry fabrication methods generally offer the advantage of easy control of patterns, but have problems with grain size, roughness and line thickness/resolution<sup>15,27</sup>. In addition, such approaches can be complicated and offer low compatibility with roll-to-roll processing, which limits their application in flexible electronics<sup>21</sup>. Wet fabrication methods, conversely, provide compatibility with the roll-to-roll processing of organic electronics<sup>2,14,20</sup>. However, they can lead to inhomogeneous distribution or aggregation of conducting substances (such as nanowires in suspension), which results in electrodes with a high percolation threshold<sup>28,29</sup> and large surface roughness and, ultimately, an overall low combined performance in terms of conductivity and transparency<sup>14,20</sup>. Furthermore, they yield uncontrolled patterns during the film formation process<sup>15,21</sup>. To improve the overall properties of solution processed FTEs,

post-treatment strategies (such as lithographic pattern-controlled methods<sup>30</sup>, pressing<sup>31</sup>, sintering or thermal annealing) have been applied<sup>32,33</sup>. However, the overall optoelectronic performance of these FTEs is still relatively limited.

With solution processes, different conductive materials, including carbon nanotubes, graphene, conducting polymers and metallic nanowires, have been explored<sup>15,21</sup>. Among these, silver nanowires (AgNWs) have been considered an attractive candidate due to their low sheet resistance ( $R_{sh}$ ), high transmittance and excellent flexibility<sup>34–36</sup>. However, AgNW-based FTEs still suffer a trade-off between conductivity and transmittance, and a large surface roughness due to the uncontrolled or random pattern of AgNWs in their film electrodes, which lead to diminished device performance and sometimes even electric short circuits<sup>14,20</sup>. To address these issues, a homogeneous AgNW distribution in suspension is required, followed by the generation of uniform and smooth FTEs with a low percolation threshold<sup>28,29</sup>. To achieve this, pattern control, such as hexagonal or square patterns of AgNWs in the FTEs similar to that of metal grid FTEs<sup>24,37</sup>, is required during the formation of the films of the AgNW suspension.

In this article, we report a strategy to achieve high-performance FTEs using a water-dispersed homogeneous suspension of AgNWs with poly(sodium 4-styrenesulfonate) (PSSNa) as a polyelectrolyte. The approach relies on ionic electrostatic charge repulsion among the AgNWs, which is due to the preferred adsorption of PSSNa anions. This leads to AgNW suspensions with stable, homogeneous dispersions. Moreover, it directly generates FTEs with grid-like patterns and high smoothness with a low percolation threshold. The approach combines the advantages of dry (pattern control) and wet (solution process) methods, and the FTEs can be fabricated in one step without any post-treatment. The resulting flexible electrodes (called FlexAgNEs) exhibit encouraging electro-optical properties ( $R_{sh} \approx 10 \Omega \square^{-1}$  with around 92% transmittance, using the substrate as the reference), film uniformity, surface smoothness

<sup>1</sup>State Key Laboratory and Institute of Elemento-Organic Chemistry, Centre of Nanoscale Science and Technology and Key Laboratory of Functional Polymer Materials, College of Chemistry, Nankai University, Tianjin, China. <sup>2</sup>School of Materials Science and Engineering, National Institute for Advanced Materials, Nankai University, Tianjin, China. \*e-mail: [yschen99@nankai.edu.cn](mailto:yschen99@nankai.edu.cn)

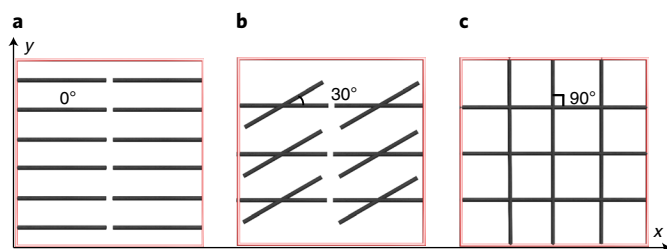


**Fig. 1 | Three typical patterns and their percolation.** a–c, Patterns of long conducting sticks (nanowires) of the same length and diameter and with the orientation determined by the cut-off angle:  $\theta = 0^\circ$  (a),  $\theta = 30^\circ$  (b) and  $\theta = 90^\circ$  (c).

and flexibility. To illustrate the potential of the approach in organic electronics, the flexible electrodes are used to create OPV devices. The OPV devices are tested with different types of donors and acceptors, and performance comparable to devices based on commercial rigid ITO electrodes is demonstrated. In particular, flexible single-junction and tandem OPV devices are demonstrated with PCEs of 13.1% and 16.5%, respectively.

### Theoretical physical model

According to percolation theory<sup>38,39</sup>, a crossed alignment strategy is considered the best approach for nanowire-based transparent conductive electrodes to achieve low sheet resistance and high optical transmittance, and the approach has been explored using various methods<sup>40,41</sup>. This strategy can be explained using a simple model (Fig. 1) where lines represent the conducting sticks, or nanowires, of the same length and diameter in a fixed loading volume. Each wire's orientation can be defined by its cut-off angle  $\theta$  ( $0$ – $90^\circ$ ) to the transverse direction, assumed to be the  $x$  axis. Three representative patterns with different values of  $\theta$  ( $0^\circ$ ,  $30^\circ$  and  $90^\circ$ ) are shown in Fig. 1a–c. In the completely anisotropic case (Fig. 1a), the aligned wires fail to create percolation paths due to the lack of intersecting wires. With increasing values of  $\theta$ , percolation paths appear in the longitudinal direction ( $y$  axis) first. Both transverse and longitudinal percolation paths emerge when  $\theta = 90^\circ$  (Fig. 1c), leading to high conductivity (in all directions) and transparency. In general, for fixed loadings, larger values of  $\theta$  would substantially increase the percolation paths, with the ideal one having a grid or square pattern ( $\theta = 90^\circ$ )<sup>38,39</sup>. In other words, for similar values of  $R_{\text{sh}}$ , the pattern of conducting sticks (nanowires) with larger values of  $\theta$  would have a lower percolation threshold, thus requiring less loading and leading to higher transmittance. Therefore, ideal grid pattern control with the minimum loading of conducting nanowires for both high conductivity and transparency is required in order to achieve high-performance FTEs with the same conducting nanowire materials<sup>28,38,39</sup>.

Previously, structural features such as preferred alignments have been achieved<sup>42</sup>, but have had problems with anisotropy and thus percolation paths of low efficiency. With a consistent electric charge on the surface of AgNWs, the nanowires could be homogeneously distributed in suspension to minimize the energy of the system on the basis of Coulomb's law<sup>43</sup>. If such charge repulsion was maintained during the film formation process, the desired square pattern with a cut-off angle of  $90^\circ$  (Fig. 1c) could be formed, if no other force was involved.

### Fabrication of FlexAgNEs and their morphology

To achieve the desired structures, we explored different positive/neutral/negative (poly)electrolyte materials (listed and summarized in Supplementary Figs. 1–3 and Supplementary Table 1), including positive-type hexadecyl trimethyl ammonium chloride, neutral-type polyvinyl alcohol (PVA), polyvinyl pyrrolidone and

polyethylene oxide, negative-type PSSNa and sodium polyacrylate (PAAS), and negative small molecular-type electrolytes such as sodium dodecyl benzene sulfonate and sodium dodecyl sulfate. As shown in Supplementary Fig. 4, clear aggregation and high roughness were always observed in the testing of a wide range of concentrations ( $0.5$ – $4 \text{ mg ml}^{-1}$ ) of AgNW suspension when no electrolyte was added.

Surprisingly, the use of positive and neutral types of electrolyte, including the polymeric and small molecular ones, did not offer clear improved performance of the fabricated FTEs (Supplementary Figs. 1b,c and 2b,c and Supplementary Table 1). When using neutral/negative small molecular electrolytes such as 2-mercaptoethanol and sodium dodecyl benzene sulfonate, there was the problem of crystallization/aggregation of the molecules when the solvent evaporated (Supplementary Figs. 1d and 2d, and Supplementary Table 1), which led to high roughness of the film and limited performance, similar to that previously reported for the preparation of copper-nanowire-based electrodes<sup>44</sup>. However, the use of polymeric electrolyte PSSNa with negative charge on the polymer chain leads to high conductivity and transparency, as well as a rather smooth surface of the FTEs (Supplementary Table 1 and Supplementary Figs. 1e and 2e). Also, as a comparison, another negative polymeric electrolyte, PAAS, was tested, but the corresponding FTEs were not as good as that from PSSNa (Supplementary Table 1).

It is easy to explain why the FTEs from neutral polyelectrolyte PVA would not be as good as expected, since there would be no (or little) charge repulsion as the interaction between the PVA molecules and AgNWs and the adsorption are also expected to be small, as it is well known that the surface of AgNWs would be positive-charge enriched<sup>44</sup>. This means that negative electrolytes such as PSSNa would be favourably adsorbed. Thus, the enriched negative charge (from the sulfonic group in the PSSNa) on AgNWs would cause the AgNWs to disperse homogeneously in water due to the same charge repulsion (Supplementary Fig. 3e). For the case of another negative polyelectrolyte, PAAS, since PAAS is a weaker electrolyte than PSSNa, the adsorption and charge density on AgNWs would be smaller, thus leading to an overall relatively weaker repulsion among the AgNWs and a lower quality of AgNW suspension and of the film prepared from it (Supplementary Table 1). As for the negative small molecular-type electrolytes, the adsorption and charge density of the small molecule electrolytes on AgNWs would be smaller than those of polymeric negative electrolytes, which could thus lead to inferior dispersion compared with those of AgNWs using polymeric electrolytes. In addition, the small molecules tend to easily crystallize/aggregate to give high roughness of the film. These results indicate that both the charge type and molecular type play important roles in achieving the desired AgNW distribution for the best electrode.

With the optimal material PSSNa selected, the FlexAgNEs, fabricated using different amounts of PSSNa with the same AgNW concentration of  $4 \text{ mg ml}^{-1}$ , were evaluated further. Compared with the electrode without PSSNa (Supplementary Fig. 5a), increasing the loading of PSSNa tends to disperse AgNWs better and causes the FlexAgNE to have a closer grid-like pattern (the crossed nanowires tend to be perpendicular to each other) when an optimal PSSNa concentration of  $10 \text{ mg ml}^{-1}$  is used (Supplementary Fig. 5c). Increasing this further to  $20 \text{ mg ml}^{-1}$  (Supplementary Fig. 5d) does not cause notable improvement in the pattern, but rather a higher resistance and lower overall performance (see below). Note that with the same initial concentration of AgNW suspensions ( $4 \text{ mg ml}^{-1}$ ), the generated FTEs with PSSNa have a lower AgNW loading on the substrate (Supplementary Fig. 6b,d) compared with the FTEs without PSSNa (Supplementary Fig. 6a,c). Even with similar AgNW coverage of 14.6% and 15.8%, the two films prepared without and with PSSNa (Fig. 2a,b) exhibit substantially different morphologies, as shown quantitatively in Supplementary Table 2. Different concentrations

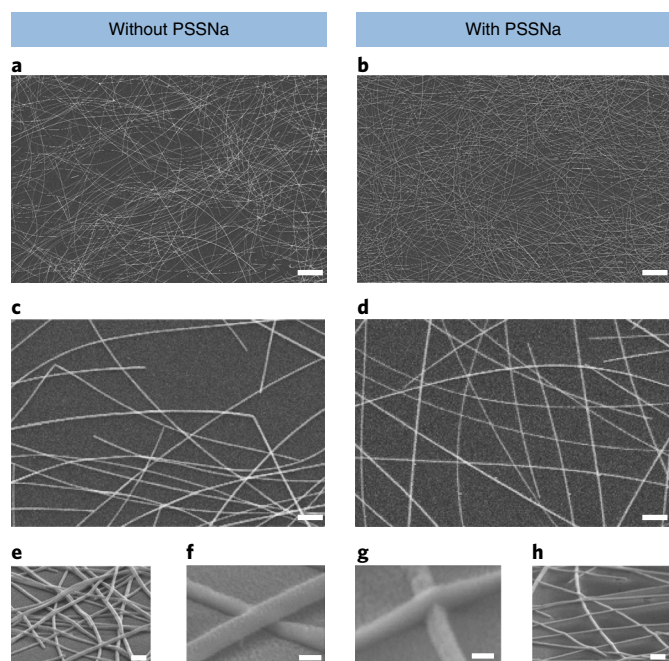


**Fig. 2 | SEM images of FlexAgNEs.** **a–d**, Surface SEM images of the films prepared from the pristine AgNW suspension ( $1 \text{ mg ml}^{-1}$ ) (**a,c**) and the AgNW suspension ( $4 \text{ mg ml}^{-1}$ ) with PSSNa ( $10 \text{ mg ml}^{-1}$ ) (**b,d**); scale bars,  $4 \mu\text{m}$  (**a,b**) and  $500 \text{ nm}$  (**c,d**). See the discussion in the text and Supplementary Table 2. **e–h**, Cross-section SEM images of the FlexAgNEs prepared from the pristine AgNW suspension ( $4 \text{ mg ml}^{-1}$ ) (**e,f**) and the AgNW suspension ( $4 \text{ mg ml}^{-1}$ ) with PSSNa ( $10 \text{ mg ml}^{-1}$ ) (**g,h**); scale bars,  $200 \text{ nm}$  (**e,h**) and  $100 \text{ nm}$  (**f,g**).

of AgNW suspensions with the same concentration of PSSNa ( $10 \text{ mg ml}^{-1}$ ) were also tested (Supplementary Fig. 7), and on the basis of these results, an optimal FlexAgNE was obtained from the suspension of AgNWs at  $4 \text{ mg ml}^{-1}$  with PSSNa ( $10 \text{ mg ml}^{-1}$ ) added.

First, the improved dispersion and close grid-like pattern when using PSSNa is mainly attributed to the ionic electrostatic charge repulsion of the enriched negative charge (from the sulfonic group in the PSSNa) adsorbed onto the surface of the AgNWs, as expected. This is supported by the observed distribution (Supplementary Fig. 8) and elemental composition (Supplementary Fig. 9) of sulfur and sodium (from PSSNa) on the surface of the AgNWs, measured by energy-dispersive spectroscopy. Further statistical analysis of cut-off angles (Supplementary Fig. 10) of the corresponding film electrodes, via statistical analysis of 100 crossed AgNW junction sites from their scanning electron microscope (SEM) images (Supplementary Fig. 1a,e), shows that the average  $\theta$  value of FlexAgNEs is  $\sim 73^\circ$  for the film prepared with PSSNa, compared with  $\sim 32^\circ$  for the film prepared without PSSNa. In addition, the average cut-off angles depend on the loading amounts of AgNWs, as shown in Supplementary Table 3. Note that the observed cut-off angle of  $\sim 73^\circ$  is not equal to the ideal of  $90^\circ$ , discussed above (Fig. 1c). This is believed to be caused by the extra shear forces and surface tension when water evaporates during the spin coating and film formation. However, fortunately, previous theoretical studies of percolation indicate that the percolation threshold does not change substantially when the cut-off angle is close to  $90^\circ$  (that is,  $70\text{--}90^\circ$ )<sup>29,39</sup>. Thus, for the case with a cut-off angle of  $73^\circ$ , obtained using PSSNa =  $10 \text{ mg ml}^{-1}$ , a pattern close to the ideal percolation threshold ( $\theta = 90^\circ$ ) should be achieved.

Even with a close-to-ideal grid-like pattern, which is expected to result in a low percolation threshold, the roughness of the FTEs

(Supplementary Tables 4 and 5) is another critical factor in their overall performance<sup>14,20</sup>. This can be achieved only when the following criteria are met: (1) AgNWs are dispersed in single-wire mode, (2) the crossing sites of nanowires are closely packed and (3) no aggregated nanoparticle (from both the conducting filler materials and electrolytes) exists. The results shown in Fig. 2d support such a single-wire mode and the absence of an aggregated nanoparticle when PSSNa was used. For the crossing sites, the junction sites of two crossing AgNWs in the FTEs prepared with/without PSSNa exhibit notable difference (Fig. 2e–h), where the former one has much closer contact than the latter one. All of these factors together cause the FlexAgNE prepared with PSSNa to have a notably lower observed roughness ( $8.2 \text{ nm}$ ) than that of  $45.1 \text{ nm}$  for the FTEs prepared without PSSNa (Supplementary Table 4 and Supplementary Fig. 11). This is also consistent with the results demonstrated by cross-section SEM images, optical images and surface profile testing (Supplementary Fig. 12). One possible reason for such close and packed contact at the crossing sites in the FlexAgNE is that the sulfonic group in the PSSNa surrounding the AgNWs would have a strong interaction with the hydroxyl groups on ozone-treated polyethylene terephthalate (PET) substrate. Another possible reason is that the capillary force caused by the evaporation of water between the two crossing wires at the junction sites can effectively push them closer due to the so-called cold welding proposed in the literature on AgNWs<sup>45</sup>.

### FlexAgNE performance

The impact of different PSSNa loadings on the properties of the obtained FlexAgNE is summarized in Fig. 3a (Supplementary Tables 5 and 6). The conductivity decreased with increasing amounts of PSSNa, whereas the transmittance increased as expected. For the optimal FlexAgNE fabricated with  $10 \text{ mg ml}^{-1}$  of PSSNa, the figure of merit (FoM)<sup>14</sup> reached a maximum value of 416 with  $R_{\text{sh}} \approx 10 \Omega \square^{-1}$  and  $\sim 92\%$  transmittance at  $550 \text{ nm}$  (excluding the substrate), demonstrating that it is among the best transparent conducting electrodes, including those based on typically deposited ITO, AgNWs, silver grids and thin metal films on flexible substrates (Fig. 3b and Supplementary Table 7). The observed high FoM here is ascribed to the grid-like pattern of the electrode (Fig. 2b,d) obtained as a consequence of both the homogeneously distributed AgNWs in suspension with PSSNa and the effect of electrostatic repulsion action in the film formation process, which is consistent with the morphological analysis discussed above.

Clearly, no or little anisotropy for such a homogeneous distribution of AgNWs and grid-like pattern in FlexAgNEs is expected. This is proved by the same observed transmittance when using polarized light with angles of  $0^\circ$  and  $90^\circ$  for the FlexAgNEs prepared with PSSNa, contrary to the notable difference in the transmittance without PSSNa and other electrolytes due to AgNW aggregations (Fig. 3c and Supplementary Figs. 13 and 14)<sup>46</sup>.

As shown in Fig. 3d, the PET/FlexAgNE including PET substrate (using air as reference) showed higher transmittance ( $\sim 85\%$ ) than the PET/pristine AgNWs ( $\sim 73\%$ ). The overall comparison between the optimized PET/FlexAgNE and that prepared without PSSNa, commercial ITO on glass/PET (Supplementary Table 8 and Supplementary Fig. 15) and the reported FTEs indicates that FlexAgNEs demonstrate superior transparency in the entire range from visible to near-infrared light. The transmittance of  $\sim 85\%$  at  $550 \text{ nm}$  for PET/FlexAgNE including PET substrate is close to that for commercial rigid ITO electrodes (Fig. 3d) and demonstrates that it has one of the best optical performances of FTEs reported to date (Supplementary Table 7). Meanwhile, the haze of PET/FlexAgNE including the substrate was determined to be low ( $1.28\%$ ).

To verify film uniformity over a large area, a FlexAgNE on PET substrate with an area of  $3.5 \text{ cm} \times 3.5 \text{ cm} = 12.25 \text{ cm}^2$  was fabricated, which exhibited a uniform distribution of transmittance and  $R_{\text{sh}}$

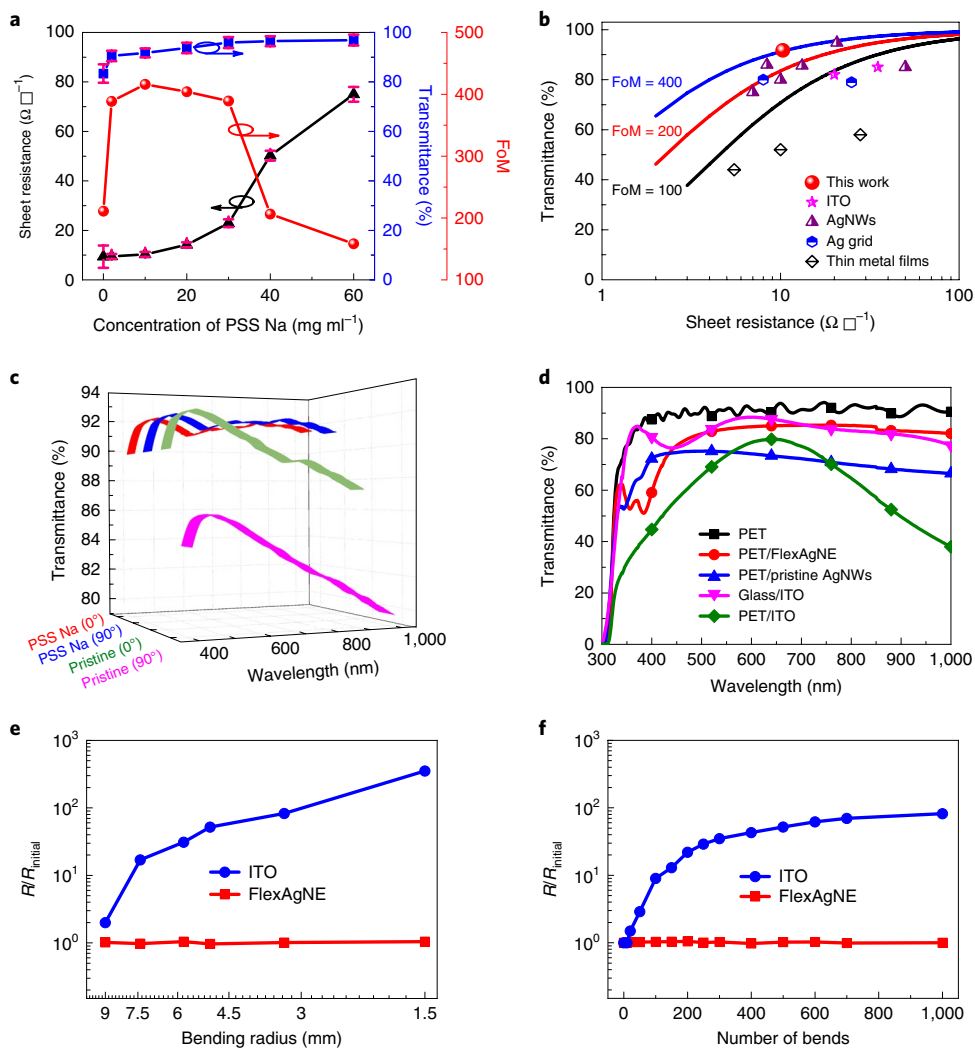


**Fig. 3 | Optoelectric and mechanical performance of FlexAgNEs.** **a**, Dependence of sheet resistance (black triangles), transmittance (blue squares) and FoM (red circles) of FlexAgNEs prepared from AgNW suspension (4 mg ml<sup>-1</sup>) with different concentrations of PSSNa (0–60 mg ml<sup>-1</sup>). The average values of sheet resistance and transmittance were calculated from more than ten electrodes. Error bars indicate the standard deviation. Circles with arrows point to relevant axes. **b**, Sheet resistance versus optical transmittance (at 550 nm) for the optimal FlexAgNE (red circle). The performances of typically reported ITO, AgNWs, silver grids and thin metal films are shown for comparison (see also Supplementary Table 7). The lines represent the values of the FoM. Note that the transmittance shown in **a** and **b** does not include the substrate (that is, using substrate as reference). **c**, Polarized transmittance of the FlexAgNEs prepared from pristine AgNW suspension (green (0°) and pink (90°) lines) and AgNW suspension with PSSNa (10 mg ml<sup>-1</sup>) (red (0°) and blue (90°) lines). **d**, Optical transmittance of the bare-PET substrate (black squares and lines), PET/FlexAgNE (red circles and lines, 10.3 Ω □<sup>-1</sup>, prepared from AgNW suspension (4 mg ml<sup>-1</sup>)), PET/pristine AgNWs (blue triangles and lines, 9.5 Ω □<sup>-1</sup>, prepared from AgNW suspension (4 mg ml<sup>-1</sup>)), glass/ITO (pink triangles and lines, 10.1 Ω □<sup>-1</sup>) and PET/ITO (green diamonds and lines, 9.5 Ω □<sup>-1</sup>). Note that the transmittance shown in **d** includes the substrate (that is, using air as reference). **e**, Increase in resistance versus bending radius for the optimal FlexAgNE (red squares) and ITO (blue circles) on PET substrates. **f**, Variation in resistance of the optimal FlexAgNE (red squares) and ITO (blue circles) films on PET substrate as a function of the number of cycles of repeated bending to a radius of 5 mm.

value, with a small standard deviation of 2 and 1.45, respectively (Supplementary Fig. 16).

Overall, the improved performance of the FlexAgNE compared with that prepared without PSSNa could be due to several factors working simultaneously. First, a homogeneously dispersed and stable suspension of AgNWs is able to form due to the above-mentioned ionic electrostatic charge repulsion. Furthermore, the even distribution of AgNWs is retained during the film formation process. Thus, a uniform film with a grid-like pattern and high smoothness with low percolation threshold can be obtained.

In addition to its superior optoelectric performance with high uniformity and smooth surface, the FlexAgNE showed good stability. Damp heat and thermal stability tests for the FlexAgNE

were carried out in air (Supplementary Fig. 17). In the case of damp heat stability, there was no change in the  $R_{sh}$  value at 85 °C and 85% relative humidity at 150 h (Supplementary Fig. 17a). The  $R_{sh}$  value showed no change at 200 °C at 120 min (Supplementary Fig. 17b), indicating good thermal stability of the FlexAgNE. As shown in Supplementary Fig. 17c, at 200 °C for 120 min, the AgNWs on the substrate remained intact, which is consistent with the unchanged  $R_{sh}$  value.

Mechanical properties of the FlexAgNE, including flexibility and durability under bending stress, were investigated. As shown in Fig. 3e, the resistance of the FlexAgNE essentially remains unchanged, with a bending radius down to 1.5 mm, contrary to the sharp 351% increase in resistance for the PET/ITO electrode.

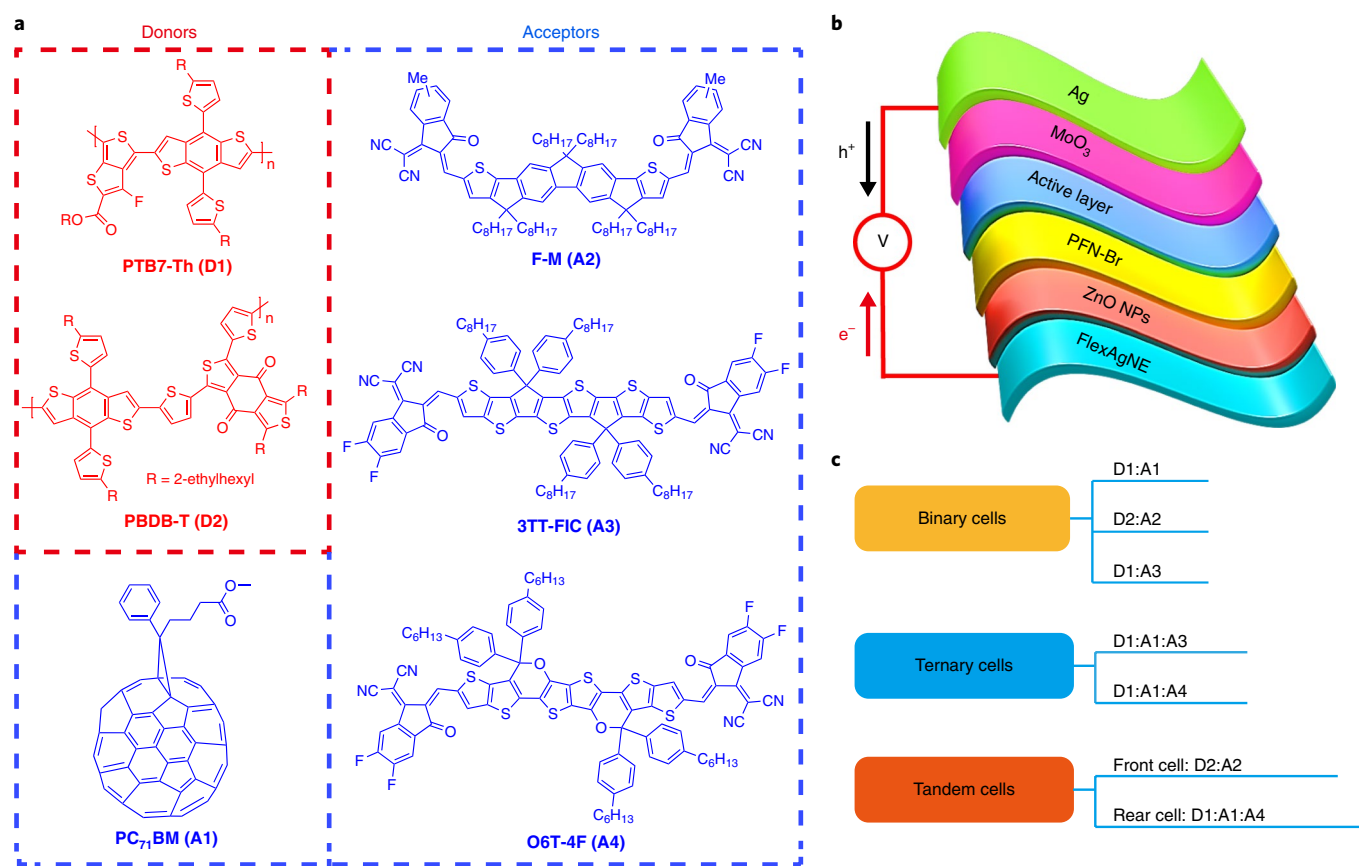


**Fig. 4 | OPV applications using FlexAgNEs. a**, Chemical structures of different types of donors and acceptors (PTB7-Th (D1), PBDB-T (D2), PC<sub>71</sub>BM (A1), F-M (A2)<sup>47</sup>, 3TT-FIC (A3)<sup>48</sup> and O6T-4F (A4)<sup>6,7</sup>) used in active layers. **b**, Schematic architecture of the flexible OPVs. **c**, Different combinations with different types of donors and acceptors for both single-junction/tandem OPV devices (single-junction binary cells: D1:A1, D2:A2 and D1:A3; single-junction ternary cells: D1:A1:A3 and D1:A1:A4; tandem cells: D2:A2 (front cell) and D1:A1:A4 (rear cell)). MoO<sub>3</sub>, molybdenum trioxide; PFN-Br, poly[(9,9-bis(3'-((N,N-dimethyl)-N-ethylammonium)-propyl)-2,7-fluorene)-alt-2,7-(9,9-dioctylfluorene)] dibromide; ZnO NPs, zinc oxide nanoparticles.

Similar results were observed for the 1,000-cycle bending test, as shown in Fig. 3f. Together with the optoelectric parameters described above, these excellent mechanical properties should make the FlexAgNE widely suitable for flexible organic electronics.

### Fabrication and performance of flexible OPVs

With the combined high-performance features of FlexAgNEs, to prove their potential application in flexible organic electronics, wider testing and studies were carried out on a series of OPVs with different types of donors and acceptors (PTB7-Th (D1), PBDB-T (D2), PC<sub>71</sub>BM (A1), F-M (A2)<sup>47</sup>, 3TT-FIC (A3)<sup>48</sup> and O6T-4F (A4)<sup>6,7</sup>) used in the active layers (Fig. 4). The detailed fabrication procedure can be found in Methods.

The results of devices based on PET/FlexAgNEs and commercial rigid ITO are summarized in Table 1. Figure 5a,b gives the typical current density versus voltage (*J*-*V*) curves for a single-junction device and a tandem cell, and the others are shown in Supplementary Fig. 18. As shown in Table 1, the devices based on FlexAgNEs all gave performance comparable to those of rigid ITO-based devices, from our own test and the literature<sup>6,7,47-49</sup>. For example, the flexible single-junction binary (D1:A1), ternary (D1:A1:A4) and tandem (D2:A2/D1:A1:A4) cells yield high PCE values of 9.82%, 13.15% and 16.55% with FlexAgNEs, respectively, which are comparable to those of ITO-based devices. The performance of two typical single-junction devices (D1:A1 and D1:A1:A4) based on FlexAgNEs and rigid ITO electrodes was certified by the National Institute of

Metrology in China (Supplementary Fig. 19). The certified flexible OPV devices based on FlexAgNEs show nearly the same performance as that based on ITO electrodes. In addition, large-area devices based on FlexAgNEs were fabricated and gave performance comparable to that based on the rigid ITO electrodes even with areas of up to 102 mm<sup>2</sup> (Supplementary Table 9). A typical external quantum efficiency curve of a single-junction (D1:A1) device based on FlexAgNEs is shown in Supplementary Fig. 20, indicating that the curve is essentially the same in terms of both pattern and values to that based on ITO. The best PCEs achieved for single-junction and tandem devices based on FlexAgNE were 13.15% and 16.55%, respectively, which are notably higher than previously reported values of 12.5% (ref. 16) and 8.34% (ref. 19) for flexible OPVs (Supplementary Table 10).

The mechanical performance of the flexible OPV devices with the FlexAgNEs on PET substrates was also studied under different bending radii (9.0 mm, 7.5 mm, 5.0 mm, 3.5 mm and 1.5 mm) and continuing the bending cycle testing of repeated bending to a radius of 5 mm. As shown in Fig. 5c, the performance of all of the tested cells remained essentially unchanged (>96% PCEs retained) with a bending radius down to 1.5 mm. As shown in Fig. 5d, the flexible OPV devices display exceptional mechanical bending stability while retaining >95% of their initial PCEs after a 1,000-cycle bending test (Supplementary Fig. 21). In addition, the three flexible OPV devices show stable behaviour, with performance degradation of 10%, 4% and 4%, respectively, after continuing testing over 70

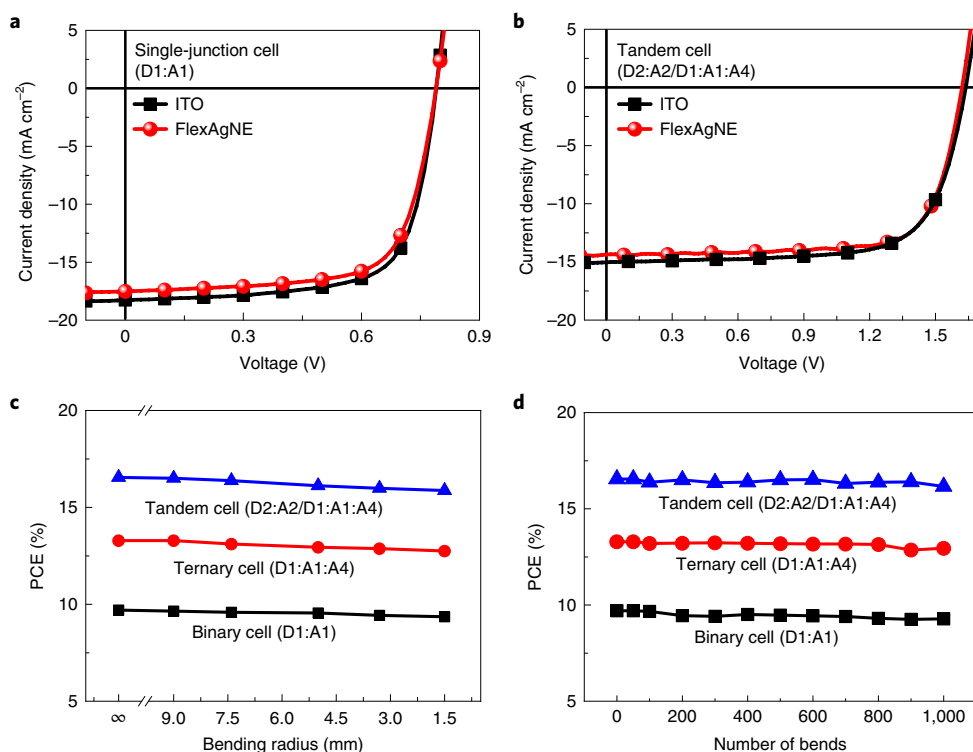


**Fig. 5 | Performance of flexible and rigid OPV devices.** **a**,  $J$ - $V$  curves of a typical single-junction device (D1:A1) based on FlexAgNEs and ITO glass electrodes. **b**,  $J$ - $V$  curves of a typical tandem device (D2:A2/D1:A1:A4) based on FlexAgNEs and ITO electrodes. **c**, PCE values for flexible OPV devices based on FlexAgNEs as a function of bending radius (9.0 mm, 7.5 mm, 5.0 mm, 3.5 mm and 1.5 mm). **d**, PCE values for flexible OPV devices based on FlexAgNEs as a function of the number of cycles of repeated bending to a radius of 5 mm.

**Table 1 | Performance parameters of the OPV devices with FlexAgNEs on PET and commercial ITO glass electrodes, together with the corresponding results from the literature on ITO for comparison**

Active layer	Electrode	$V_{oc}$ (V)	$J_{sc}$ (mA cm <sup>-2</sup> )	FF (%)	PCE (%) <sup>c</sup>	Refs.
D1:A1	FlexAgNE <sup>a</sup>	0.795 ± 0.012(0.802)	17.23 ± 0.42(17.43)	70.20 ± 0.02(70.2)	9.64 ± 0.48(9.82)	
	ITO <sup>a</sup>	0.796 ± 0.008(0.799)	17.93 ± 0.17(18.00)	69.80 ± 0.69(70.4)	9.89 ± 0.35(10.12)	
	ITO <sup>b</sup>	0.815	17.52	72.0	10.28	49
D2:A2	FlexAgNE <sup>a</sup>	0.938 ± 0.010(0.940)	15.76 ± 0.45(15.92)	68.86 ± 0.96(69.5)	10.29 ± 0.23(10.40)	
	ITO <sup>a</sup>	0.938 ± 0.002(0.940)	15.86 ± 0.25(15.96)	69.67 ± 0.56(69.8)	10.38 ± 0.17(10.47)	
	ITO <sup>b</sup> -I	0.934 ± 0.005(0.938)	15.86 ± 0.12(15.96)	69.20 ± 0.50(69.8)	10.25 ± 0.14(10.45)	6
	ITO <sup>b</sup> -C	0.986	14.86	70.0	10.26	47
D1:A3	FlexAgNE <sup>a</sup>	0.665 ± 0.008(0.663)	25.67 ± 0.13(25.68)	70.50 ± 0.86(71.0)	11.98 ± 0.25(12.09)	
	ITO <sup>a</sup>	0.664 ± 0.003(0.662)	25.54 ± 0.16(25.71)	69.98 ± 0.92(71.2)	12.11 ± 0.13(12.12)	
	ITO <sup>b</sup>	0.662	25.89	71.2	11.96 ± 0.25(12.21)	48
D1:A1:A3	FlexAgNE <sup>a</sup>	0.667 ± 0.007(0.669)	26.90 ± 0.43(27.02)	71.14 ± 0.94(71.8)	12.76 ± 0.50(12.98)	
	ITO <sup>a</sup>	0.667 ± 0.005(0.668)	26.97 ± 0.52(27.56)	71.54 ± 1.06(72.0)	13.21 ± 0.08(13.26)	
	ITO <sup>b</sup>	0.669	27.73	73.0	13.33 ± 0.21(13.54)	48
D1:A1:A4	FlexAgNE <sup>a</sup>	0.696 ± 0.008(0.699)	26.85 ± 0.23(26.99)	69.45 ± 0.95(69.7)	13.02 ± 0.23(13.15)	
	ITO <sup>a</sup>	0.697 ± 0.005(0.702)	27.07 ± 0.13(27.08)	69.35 ± 0.80(69.9)	13.08 ± 0.20(13.30)	
	ITO <sup>b</sup>	0.689 ± 0.004(0.691)	27.98 ± 0.35(27.60)	68.6 ± 0.6(69.7)	13.22 ± 0.23(13.29)	6
	ITO <sup>b</sup>	0.70	28.20	71.0	14.08	7
D2:A2/D1:A1:A4	FlexAgNE <sup>a</sup>	1.628 ± 0.012(1.640)	13.99 ± 0.23(14.22)	69.70 ± 1.30(71.0)	16.01 ± 0.50(16.55)	
	ITO <sup>b</sup>	1.636 ± 0.014(1.642)	14.32 ± 0.18(14.35)	72.1 ± 1.4(73.7)	16.89 ± 0.29(17.36)	6

$J_{sc}$ , short-circuit current density;  $V_{oc}$ , open-circuit voltage; FF, fill factor. <sup>a</sup>Statistical average and error bars of standard deviation from the average values of OPV parameters for FlexAgNEs and ITO electrodes are listed outside parentheses, and the best optimal results are listed inside parentheses, respectively. <sup>b</sup>Cited from refs. 6,747-49 (ITO<sup>b</sup>-I: the device architecture is ITO/ZnO/PFN-Br/D2:A2/M-PEDOT/Ag; ITO<sup>b</sup>-C: the device architecture is ITO/PEDOT:PSS/D2:A2/PDINO/Al). <sup>c</sup>The average parameters were calculated from more than 20 devices.

days (Supplementary Fig. 22), similar to that previously reported for ITO-based devices<sup>6,50</sup>.

## Conclusions

We have reported a strategy to create grid-like, smooth, flexible electrodes. Our solution process uses water suspension of AgNWs, with PSSNa as the polyelectrolyte, and can prepare FTEs in a single step without any post-treatment. The electrodes offer encouraging optoelectric properties, film uniformity, smoothness and flexibility. To illustrate the capabilities of the approach, the electrodes were used to create flexible OPV devices, which exhibited performance comparable to devices on commercial ITO glass electrodes. The flexible single-junction and tandem OPV devices demonstrated PCEs of 13.1% and 16.5%, respectively. Our flexible electrodes should also be of use with other flexible organic electronic devices, including light-emitting diodes and transistors. The strategy, which is based on electrostatic repulsion, could also be used to prepare dispersions and flexible electrodes based on other conducting filler materials such as different metals and nanostructured carbon.

## Methods

**Materials.** All materials were used as obtained unless otherwise indicated. AgNWs (10 wt% in H<sub>2</sub>O with an average length of ~25 μm and diameter of ~25 nm) were purchased from Zhejiang Kechuang Advanced Materials. Glass/ITO and PET/ITO were purchased from Liaoning Advanced Election Technology. PSSNa (weight-averaged molecular mass of 70,000, powder) and other electrolytes were purchased from Sigma-Aldrich. PTB7-Th (D1, also called PCE10) was purchased from 1-Material. PBDB-T (D2) was purchased from Solarmer Material. F-M (A2), 3TT-FIC (A3) and O6T-4F (A4) were synthesized according to the literature<sup>7,47,48</sup>. ZnO nanoparticles were synthesized following ref. <sup>51</sup>.

**Fabrication of FlexAgNEs.** Before fabrication, the PET substrate was treated by ultraviolet ozone for 10 min. Then, the water suspension of AgNWs without and with different electrolytes were spin coated. For the optimal FlexAgNE, first, AgNWs (10 wt% in H<sub>2</sub>O) were diluted in deionized water to create a 4 wt% water suspension. Then, 10 ml AgNWs (4 wt% in H<sub>2</sub>O) were mixed with 0.01 ml PSSNa aqueous solution (1,000 mg ml<sup>-1</sup>). The mixed suspension (100 μl) was spin coated on PET at a spin speed of 1,000 r.p.m. for 60 s to afford the FlexAgNEs.

**Electrode characterization.** The surface and cross-section morphologies of AgNW films were measured by SEM (ZEISSMERLIN Compact). A transmission electron microscope (JEOL JEM-2800) and energy-dispersive spectrometer (JEOL JEM-2800) were used to investigate the elemental mapping and composition of AgNW films. The roughness of AgNW films was measured using an atomic force microscope (Bruker MultiMode 8), focused ion beam/SEM (FEI-Helios NanoLab 460HP) and a Veeco Dektak 150 profilometer. The optical images for AgNW-based electrodes were obtained from the Veeco Dektak 150 profilometer.

Polarized transmittance spectra were measured using a HITACHI U-4100 spectrophotometer. Six points at different positions on the same film (~2 cm × 2 cm) with and without PSSNa were measured with a beam size of 2 mm × 4 mm. The electrode transmittance was measured with a JASCO V-570 spectrophotometer. An identical PET was used for reference, to evaluate the intrinsic transmittance of the AgNW film. In addition, the transmittance of the flexible electrode based on PET was measured using air as reference (see the references in Supplementary Table 11). The haze values of FlexAgNEs were obtained with a WGW Haze meter, and all haze measurements include the substrate (that is, using air as reference).

Sheet resistance of the AgNW films was measured on a ST-2258C four-probe instrument (Suzhou Jingge Electronic).

The optoelectric performance of the FTEs was evaluated by the FoM, defined as  $\sigma_{dc}/\sigma_{op}(\lambda)$  in equation (1)<sup>14</sup>:

$$T = \left( 1 + \frac{Z_0 \sigma_{op}(\lambda)}{2R_{sh} \sigma_{dc}} \right)^{-2} \quad (1)$$

where  $Z_0$  is the impedance of free space ( $Z_0 = 377 \Omega$ ),  $\sigma_{dc}$  and  $\sigma_{op}(\lambda)$  are the direct-current and optical conductivities of the materials, respectively, and the transmittance of the FTEs,  $T$ , was measured at a wavelength,  $\lambda$ , of 550 nm, which is representative of the maximum response of the human eye. With the measured transmittance, the value of  $R_{sh}$  followed by that of FoM =  $\sigma_{dc}/\sigma_{op}(\lambda)$  can be obtained from equation (1).

**Fabrication of OPV devices.** The flexible single-junction and tandem OPV devices were all fabricated using the same standard solution process method as that

for the commercial ITO glass previously reported<sup>6,7,47–49</sup>. The following gives details of two typical samples.

For single-junction devices, ZnO nanoparticles<sup>51</sup> were spin coated on top of the FlexAgNE at 3,000 r.p.m. for 40 s at room temperature. Subsequently, a thin layer of poly[(9,9-bis(3'-(N,N-dimethyl)-N-ethylammonium)-propyl)-2,7-fluorene]-alt-2,7-(9,9-dioctylfluorene)] dibromide (PFN-Br; 1 mg ml<sup>-1</sup> in methanol) was spin coated at 3,000 r.p.m. for 40 s on the ZnO for improving the interfacial properties. The substrates were then transferred to an argon-filled glove box. Then, different binary (D1:A1 and D1:A3) and ternary (D1:A1:A3 and D1:A1:A4) blend solutions were spin coated separately according to the recipe in Supplementary Table 12, to form the active layers. Finally, a MoO<sub>3</sub> layer (6 nm) and a Ag layer (70 nm) were then deposited on the active layer by vacuum evaporation at  $2 \times 10^{-4}$  Pa. The device architecture based on D2:A2 is FlexAgNE/ZnO NPs/PFN-Br/PBDB-T:F-M/M-PEDOT/Ag, which was also used for the following fabrication of tandem devices. The effective areas of cells were ~4 mm<sup>2</sup>, defined by shallow masks.

The tandem device was fabricated with an architecture of FlexAgNE/ZnO NPs/PFN-Br/D2:A2/M-PEDOT/ZnO/D1:A1:A4/MoO<sub>3</sub>/Ag. First, D2:A2 was spin coated at 1,000 r.p.m. for 40 s on the substrate of the FlexAgNE, with ZnO nanoparticles and PFN-Br in the same way as the single-junction devices described above. Subsequently, the M-PEDOT layer (Clevious P VP Al 4083, diluted with an equal volume of isopropyl alcohol and 0.3 wt% of Zonyl FSN, ~50 nm) was spin coated on top of the active layer of the front subcell, followed by annealing at 120 °C for 10 min, and then a layer of ZnO nanoparticles (~15 nm) was spin coated and annealed at 120 °C for 10 min in the glove box. Then, the D1:A1:A4 active layers were spin coated at 1,600 r.p.m. for 40 s. The tandem device was completed by deposition of a MoO<sub>3</sub> layer (~6 nm) and Ag layer (~70 nm) at  $2 \times 10^{-4}$  Pa. The effective areas of cells were ~4 mm<sup>2</sup>, defined by shallow masks.

**Device characterization.** The  $J$ - $V$  curves of fabricated devices were obtained by a Keithley 2400 source-measure unit. The photocurrent was measured under AM1.5G (air mass 1.5 global) illumination at 100 mW cm<sup>-2</sup> irradiation using an Enli SS-F5-3A solar simulator, calibrated with a standard Si solar cell (Enli Technology, and the calibrated report can be traced to the National Renewable Energy Laboratory). The scan speed and dwell times of the  $J$ - $V$  curves were fixed at 0.015 V s<sup>-1</sup> and 20 ms, respectively. The external quantum efficiency spectrum was measured using a QE-R Solar Cell Spectral Response Measurement System (Enli Technology).

**Reporting Summary.** Further information on research design is available in the Nature Research Reporting Summary linked to this article.

## Data availability

The data that support the plots within this paper and other findings of this study are available from the corresponding author upon reasonable request.

Received: 24 December 2018; Accepted: 18 September 2019;  
Published online: 4 November 2019

## References

- Forrest, S. R. The path to ubiquitous and low-cost organic electronic appliances on plastic. *Nature* **428**, 911–918 (2004).
- Angmo, D., Larsen-Olsen, T. T., Jørgensen, M., Søndergaard, R. R. & Krebs, F. C. Roll-to-roll inkjet printing and photonic sintering of electrodes for ITO free polymer solar cell modules and facile product integration. *Adv. Energy Mater.* **3**, 172–175 (2012).
- Park, S. et al. Self-powered ultra-flexible electronics via nano-grating-patterned organic photovoltaics. *Nature* **561**, 516–521 (2018).
- Ellmer, K. Past achievements and future challenges in the development of optically transparent electrodes. *Nat. Photon.* **6**, 809–817 (2012).
- Hou, J., Inganas, O., Friend, R. H. & Gao, F. Organic solar cells based on non-fullerene acceptors. *Nat. Mater.* **17**, 119–128 (2018).
- Meng, L. et al. Organic and solution-processed tandem solar cells with 17.3% efficiency. *Science* **361**, 1094–1098 (2018).
- Xiao, Z., Jia, X. & Ding, L. Ternary organic solar cells offer 14% power conversion efficiency. *Sci. Bull.* **62**, 1562–1564 (2017).
- Kan, B. et al. A chlorinated low-bandgap small-molecule acceptor for organic solar cells with 14.1% efficiency and low energy loss. *Sci. China Chem.* **61**, 1307–1313 (2018).
- Tonzani, S. Time to change the bulb. *Nature* **459**, 312–314 (2009).
- Sirringhaus, H. 25th anniversary article: organic field-effect transistors: the path beyond amorphous silicon. *Adv. Mater.* **26**, 1319–1335 (2014).
- Traverse, C. J., Pandey, R., Barr, M. C. & Lunt, R. R. Emergence of highly transparent photovoltaics for distributed applications. *Nat. Energy* **2**, 849–860 (2017).
- Chen, D., Liang, J. & Pei, Q. Flexible and stretchable electrodes for next generation polymer electronics: a review. *Sci. China Chem.* **59**, 659–671 (2016).

13. Rogers, J. A., Someya, T. & Huang, Y. G. Materials and mechanics for stretchable electronics. *Science* **327**, 1603–1607 (2010).
14. Langley, D. et al. Flexible transparent conductive materials based on silver nanowire networks: a review. *Nanotechnology* **24**, 452001 (2013).
15. Li, Y. W., Xu, G. Y., Cui, C. H. & Li, Y. F. Flexible and semitransparent organic solar cells. *Adv. Energy Mater.* **8**, 1701791 (2018).
16. Xiong, S. et al. 12.5% flexible nonfullerene solar cells by passivating the chemical interaction between the active layer and polymer interfacial layer. *Adv. Mater.* **31**, 1806616 (2019).
17. Spyropoulos, G. D. et al. Flexible organic tandem solar modules with 6% efficiency: combining roll-to-roll compatible processing with high geometric fill factors. *Energy Environ. Sci.* **7**, 3284–3290 (2014).
18. Kang, H., Jung, S., Jeong, S., Kim, G. & Lee, K. Polymer-metal hybrid transparent electrodes for flexible electronics. *Nat. Commun.* **6**, 6503 (2015).
19. Luo, B. et al. Colorful flexible polymer tandem solar cells. *J. Mater. Chem. C* **5**, 7884–7889 (2017).
20. Sannicolo, T. et al. Metallic nanowire-based transparent electrodes for next generation flexible devices: a review. *Small* **12**, 6052–6075 (2016).
21. Cao, W. R., Li, J., Chen, H. Z. & Xue, J. G. Transparent electrodes for organic optoelectronic devices: a review. *J. Photon. Energy* **4**, 040990 (2014).
22. Park, S., Vosguerichian, M. & Bao, Z. A. A review of fabrication and applications of carbon nanotube film-based flexible electronics. *Nanoscale* **5**, 1727–1752 (2013).
23. Bae, S. et al. Roll-to-roll production of 30-inch graphene films for transparent electrodes. *Nat. Nanotechnol.* **5**, 574–578 (2010).
24. Ahn, B. Y. et al. Omnidirectional printing of flexible, stretchable, and spanning silver microelectrodes. *Science* **323**, 1590–1593 (2009).
25. Jiang, Z. et al. Reverse-offset printed ultrathin Ag mesh for robust conformal transparent electrodes for high-performance organic photovoltaics. *Adv. Mater.* **30**, 1707526 (2018).
26. Wu, H. et al. A transparent electrode based on a metal nanotrough network. *Nat. Nanotechnol.* **8**, 421–425 (2013).
27. Gu, D., Zhang, C., Wu, Y.-K. & Guo, L. J. Ultrasoft and thermally stable silver-based thin films with subnanometer roughness by aluminum doping. *ACS Nano* **8**, 10343–10351 (2014).
28. Shante, V. K. S. & Kirkpatrick, S. An introduction to percolation theory. *Adv. Phys.* **20**, 325–357 (1971).
29. Scardaci, V., Coull, R., Lyons, P. E., Rickard, D. & Coleman, J. N. Spray deposition of highly transparent, low-resistance networks of silver nanowires over large areas. *Small* **7**, 2621–2628 (2011).
30. Tvingstedt, K. & Inganäs, O. Electrode grids for ITO free organic photovoltaic devices. *Adv. Mater.* **19**, 2893–2897 (2007).
31. Tokuno, T. et al. Fabrication of silver nanowire transparent electrodes at room temperature. *Nano Res.* **4**, 1215–1222 (2011).
32. Garnett, E. C. et al. Self-limited plasmonic welding of silver nanowire junctions. *Nat. Mater.* **11**, 241–249 (2012).
33. Lee, J., Lee, I., Kim, T.-S. & Lee, J.-Y. Efficient welding of silver nanowire networks without post-processing. *Small* **9**, 2887–2894 (2013).
34. Seo, J. H. et al. Cold isostatic-pressured silver nanowire electrodes for flexible organic solar cells via room-temperature processes. *Adv. Mater.* **29**, 1701479 (2017).
35. Liang, J. et al. Intrinsically stretchable and transparent thin-film transistors based on printable silver nanowires, carbon nanotubes and an elastomeric dielectric. *Nat. Commun.* **6**, 7647 (2015).
36. Narayanan, S., Hajzuz, J. R., Treacy, C. E., Bockstaller, M. R. & Porter, L. M. Polymer embedded silver-nanowire network structures—a platform for the facile fabrication of flexible transparent conductors. *ECS J. Solid State Sci. Technol.* **3**, 363–369 (2014).
37. Hösel, M., Søndergaard, R. R., Jørgensen, M. & Krebs, F. C. Fast inline roll-to-roll printing for indium-tin-oxide-free polymer solar cells using automatic registration. *Energy Technol.* **1**, 102–107 (2013).
38. Balberg, I. & Binenbaum, N. Computer study of the percolation threshold in a two-dimensional anisotropic system of conducting sticks. *Phys. Rev. B* **28**, 3799–3812 (1983).
39. De, S. & Coleman, J. N. The effects of percolation in nanostructured transparent conductors. *MRS Bull.* **36**, 774–781 (2011).
40. Yang, B. et al. Hybrid effect of crossed alignment and multi-stacking structure on the percolation behavior of silver nanowire networks. *J. Disp. Technol.* **11**, 625–629 (2015).
41. Cho, S. et al. Large-area cross-aligned silver nanowire electrodes for flexible, transparent, and force-sensitive mechanochromic touch screens. *ACS Nano* **11**, 4346–4357 (2017).
42. Hu, H., Pauly, M., Felix, O. & Decher, G. Spray-assisted alignment of layer-by-layer assembled silver nanowires: a general approach for the preparation of highly anisotropic nano-composite films. *Nanoscale* **9**, 1307–1314 (2017).
43. Allakhverdiv, G. R. Coulomb interaction in electrolyte solutions. *Dokl. Phys.* **57**, 221–223 (2012).
44. Yin, Z. et al. Copper nanowire dispersion through an electrostatic dispersion mechanism for high-performance flexible transparent conducting films and optoelectronic devices. *ACS Appl. Mater. Interfaces* **11**, 5264–5275 (2019).
45. Liu, Y. et al. Capillary-force-induced cold welding in silver-nanowire-based flexible transparent electrodes. *Nano Lett.* **17**, 1090–1096 (2017).
46. Chen, Y.-R., Hong, C.-C., Liou, T.-M., Hwang, K. C. & Guo, T.-F. Roller-induced bundling of long silver nanowire networks for strong interfacial adhesion, highly flexible, transparent conductive electrodes. *Sci. Rep.* **7**, 16662 (2017).
47. Zhang, Y. et al. Nonfullerene tandem organic solar cells with high performance of 14.11%. *Adv. Mater.* **30**, 1707508 (2018).
48. Gao, H.-H. et al. A new nonfullerene acceptor with near infrared absorption for high performance ternary-blend organic solar cells with efficiency over 13%. *Adv. Sci.* **5**, 1800307 (2018).
49. He, Z. et al. Single-junction polymer solar cells with high efficiency and photovoltage. *Nat. Photonics* **9**, 174–179 (2015).
50. Huang, W. et al. A facile approach to alleviate photochemical degradation in high efficiency polymer solar cells. *J. Mater. Chem. A* **3**, 16313–16319 (2015).
51. Beek, W. J. E., Wienk, M. M., Kemerink, M., Yang, X. & Janssen, R. A. J. Hybrid zinc oxide conjugated polymer bulk heterojunction solar cells. *J. Phys. Chem. B* **109**, 9505–9516 (2005).

## Acknowledgements

We gratefully acknowledge financial support from MoST (2016YFA0200200), NSFC (91633301, 21421001, 51873089, 51773095) of China, Tianjin city (17JCJQC44500, 17JCZDJC31100) and 111 Project (B12015).

## Author contributions

Y.C. conceived and designed the research. Y.S. fabricated the FlexAgNEs and flexible OPV devices and carried out all of the performance studies. L.M. and Y.Z. fabricated and characterized the OPV devices based on rigid ITO electrodes. M.C. and H.G. synthesized 3TT-FIC and O6T-4F. K.Z. and Y.S. built the theoretical physical model. Z.S., S.L., H.W. and J.L. conducted partial characterization of the FlexAgNEs. The manuscript was mainly prepared by Y.C., Y.S., C.L. and X.W., and all authors participated in the manuscript preparation and commented on the manuscript.

## Competing interests

A patent (application no. 201910514527.9) has been filed for the flexible electrodes and devices.

## Additional information

**Supplementary information** is available for this paper at <https://doi.org/10.1038/s41928-019-0315-1>.

**Correspondence and requests for materials** should be addressed to Y.C.

**Reprints and permissions information** is available at [www.nature.com/reprints](http://www.nature.com/reprints).

**Publisher's note** Springer Nature remains neutral with regard to jurisdictional claims in published maps and institutional affiliations.

© The Author(s), under exclusive licence to Springer Nature Limited 2019

## Solar Cells Reporting Summary

Nature Research wishes to improve the reproducibility of the work that we publish. This form is intended for publication with all accepted papers reporting the characterization of photovoltaic devices and provides structure for consistency and transparency in reporting. Some list items might not apply to an individual manuscript, but all fields must be completed for clarity.

For further information on Nature Research policies, including our [data availability policy](#), see [Authors & Referees](#).

## ► Experimental design

## Please check: are the following details reported in the manuscript?

## 1. Dimensions

- Area of the tested solar cells  Yes  No Shadow masks were used to define the device area (0.0405 cm<sup>2</sup>) of the devices.
- Method used to determine the device area  Yes  No The device area was determined using an optical profilometer.

## 2. Current-voltage characterization

- Current density-voltage (J-V) plots in both forward and backward direction  Yes  No Generally, organic photovoltaic devices do not have forward and backward problems. The current-voltage (J-V) plots in forward direction is supplied in Figure 5a, b and Supplementary Figure 18.
- Voltage scan conditions  Yes  No The scan speed and dwell times of the J-V curves were fixed at 0.015 V s<sup>-1</sup> and 20 ms, respectively as shown in Section "Device characterization".  
*For instance: scan direction, speed, dwell times*
- Test environment  Yes  No Our devices were characterized at room temperature (ca. 25 Celsius degree) in Ar glove box.  
*For instance: characterization temperature, in air or in glove box*
- Protocol for preconditioning of the device before its characterization  Yes  No No preconditioning protocol.
- Stability of the J-V characteristic  Yes  No Stability of J-V characteristic has not been conducted.  
*Verified with time evolution of the maximum power point or with the photocurrent at maximum power point; see ref. 7 for details.*

## 3. Hysteresis or any other unusual behaviour

- Description of the unusual behaviour observed during the characterization  Yes  No No hysteresis or other unusual behaviour was observed during the characterization of the solar cells. Generally, organic photovoltaic devices do not have hysteresis problems.
- Related experimental data  Yes  No No hysteresis or other unusual behaviour.

## 4. Efficiency

- External quantum efficiency (EQE) or incident photons to current efficiency (IPCE)  Yes  No The different types of devices on our FlexAgNEs all gave excellent and comparable performance compared with the devices using the commercial ITO electrodes and we have reported the devices on ITO glass in our previous work (Adv Mater, 30, 2018, 1707508; Adv Sci, 2018, 5, 1800307; Science, 2018, 361, 1094). One typical external quantum efficiency (EQE) curve of single-junction (D1:A1) device on FlexAgNE was shown in Supplementary Figure 20, and it can be seen that the curve is essential the same in both pattern and values to that on ITO.
- A comparison between the integrated response under the standard reference spectrum and the response measure under the simulator  Yes  No One typical EQE curve of single-junction (D1:A1) device on FlexAgNE was shown in Supplementary Figure 20, and the integrated current density was 16.70 and 16.66 mA-cm<sup>-2</sup> based devices with FlexAgNE on PET and ITO commercial electrode, respectively, which are consistent with the J-V measurements (17.43 and 18.0 mA-cm<sup>-2</sup>). Also the mismatch using FlexAgNE is 4.2%, similar to that (7.4%) on ITO.
- For tandem solar cells, the bias illumination and bias voltage used for each subcell  Yes  No Here, we didn't measure the flexible tandem device on FlexAgNE with bias illumination and bias voltages because we have measured the device on ITO glass in our previous work (Science, 2018, 361, 1094).

## 5. Calibration

- Light source and reference cell or sensor used for the characterization  Yes  No The light source is an Enli SS-F5-3A solar simulator (AM 1.5G illumination at 100 mW/cm<sup>2</sup> irradiation), and the reference cell is a standard Si solar cell (Enli Technology Co., Ltd., Taiwan) as shown in Section "Device characterization".
- Confirmation that the reference cell was calibrated and certified  Yes  No The calibrated report of the standard Si solar cell we used can be traced to NREL as shown in Section "Device characterization".
- Calculation of spectral mismatch between the reference cell and the devices under test  Yes  No The mismatch factor M values of one typical single-junction (D1:A1) device on FlexAgNE on PET and the commercial ITO electrode on glass substrate under the solar simulator are calculated according to the reference and the values are around 1 (1.006 for the rigid device and 1.005 for the flexible device).

## 6. Mask/aperture

- Size of the mask/aperture used during testing  Yes  No We did not use a mask during testing and the device effective area was obtained by its crossed area of the bottom and top electrodes.
- Variation of the measured short-circuit current density with the mask/aperture area  Yes  No We did not use a mask during testing .

## 7. Performance certification

- Identity of the independent certification laboratory that confirmed the photovoltaic performance  Yes  No The device performance with two typical single-junction devices (D1:A1 and D1:A1:A4) on FlexAgNE and rigid ITO electrodes were certified by the National Institute of Metrology (NIM) of China (Supplementary Fig. 19) and the certified flexible OPV devices on FlexAgNE show nearly the same performances compared with those on rigid ITO electrodes.
- A copy of any certificate(s)  
*Provide in Supplementary Information*  Yes  No The copy of certificate(s) from the National Institute of Metrology (NIM), China were shown in Supplementary Figure 19.

## 8. Statistics

- Number of solar cells tested  Yes  No The average parameters were calculated from more than 20 devices as shown in Table 1.
- Statistical analysis of the device performance  Yes  No Statistical average and error bars of standard deviation from the average values of PCEs are listed in Table 1.

## 9. Long-term stability analysis

- Type of analysis, bias conditions and environmental conditions  
*For instance: illumination type, temperature, atmosphere humidity, encapsulation method, preconditioning temperature*  Yes  No Long-term stability analysis with devices were stored in Ar glove box without encapsulation as shown in Supplementary Figure 22.